

## Investigation of a clinical PET detector module design that employs large-area avalanche photodetectors

This article has been downloaded from IOPscience. Please scroll down to see the full text article.

2011 Phys. Med. Biol. 56 3603

(<http://iopscience.iop.org/0031-9155/56/12/010>)

View [the table of contents for this issue](#), or go to the [journal homepage](#) for more

Download details:

IP Address: 128.12.220.100

The article was downloaded on 29/05/2011 at 20:24

Please note that [terms and conditions apply](#).

## Investigation of a clinical PET detector module design that employs large-area avalanche photodetectors

Hao Peng<sup>1,2,3</sup>, Peter D Olcott<sup>1,2</sup>, Virginia Spanoudaki<sup>1,2</sup> and Craig S Levin<sup>1,2,4,5</sup>

<sup>1</sup> Department of Radiology, Stanford University, Stanford, CA 94305, USA

<sup>2</sup> Molecular Imaging Program at Stanford (MIPS), Stanford, CA 94305, USA

<sup>3</sup> Department of Medical Physics, McMaster University, Ontario L8S 4K1, Canada

<sup>4</sup> Department of Physics, Stanford University, Stanford, CA 94305, USA

<sup>5</sup> Department of Electrical Engineering, Stanford University, Stanford, CA 94305, USA

E-mail: [penghao@mcmaster.ca](mailto:penghao@mcmaster.ca) and [cslevin@stanford.edu](mailto:cslevin@stanford.edu)

Received 31 January 2011, in final form 19 April 2011

Published 25 May 2011

Online at [stacks.iop.org/PMB/56/3603](http://stacks.iop.org/PMB/56/3603)

### Abstract

We investigated the feasibility of designing an Anger-logic PET detector module using large-area high-gain avalanche photodiodes (APDs) for a brain-dedicated PET/MRI system. Using Monte Carlo simulations, we systematically optimized the detector design with regard to the scintillation crystal, optical diffuser, surface treatment, layout of large-area APDs, and signal-to-noise ratio (SNR, defined as the 511 keV photopeak position divided by the standard deviation of noise floor in an energy spectrum) of the APD devices. A detector prototype was built comprising an  $8 \times 8$  array of  $2.75 \times 3.00 \times 20.0$  mm<sup>3</sup> LYSO (lutetium-yttrium-orthosilicate) crystals and a  $22.0 \times 24.0 \times 9.0$  mm<sup>3</sup> optical diffuser. From the four designs of the optical diffuser tested, two designs employing a slotted diffuser are able to resolve all 64 crystals within the block with good uniformity and peak-to-valley ratio. Good agreement was found between the simulation and experimental results. For the detector employing a slotted optical diffuser, the energy resolution of the global energy spectrum after normalization is  $13.4 \pm 0.4\%$ . The energy resolution of individual crystals varies between  $11.3 \pm 0.3\%$  and  $17.3 \pm 0.4\%$ . The time resolution varies between  $4.85 \pm 0.04$  (center crystal),  $5.17 \pm 0.06$  (edge crystal), and  $5.18 \pm 0.07$  ns (corner crystal). The generalized framework proposed in this work helps to guide the design of detector modules for selected PET system configurations, including scaling the design down to a preclinical PET system, scaling up to a whole-body clinical scanner, as well as replacing APDs with other novel photodetectors that have higher gain or SNR such as silicon photomultipliers.

(Some figures in this article are in colour only in the electronic version)

## 1. Introduction

The integration of PET and MRI has recently attracted intensive research interest because of its potential to correlate high-sensitivity molecular information from PET images with high-resolution anatomical information from MRI images (Schlemmer *et al* 2008, Pichler *et al* 2010). One promising application for PET/MRI is in neurological imaging, such as detecting small foci, diagnosing Alzheimer's and Parkinson's diseases, and correlating functional MRI with  $^{15}\text{O}$  PET (currently accepted as gold standard) in cerebral blood flow (CBF) and cerebral blood volume (CBV) measurements (Catana *et al* 2008, Judenhofer *et al* 2008). Another appealing prospect is whole body PET/MRI for oncology and cardiology studies (Takasawa *et al* 2005, Nekolla *et al* 2009). Besides several technical challenges such as physical compatibility, magnetic field inhomogeneity and electromagnetic interferences between PET and MRI components, finding a high-performance MRI compatible PET detector is critical.

As conventional photomultiplier tube (PMT) devices cannot maintain normal performances even in the relatively weak earth magnetic field of around 5 mT (Peng *et al* 2010a, 2010b), they are not considered ideal candidates for the PET/MRI design unless long optical fiber bundles are used (Shao *et al* 1997). A new photodetector type, the avalanche photodiode (APD), has been increasingly used in pre-clinical PET and PET/MRI systems (Lecomte *et al* 1990, Ziegler *et al* 2001, Pichler *et al* 2001). APDs are semiconductor detectors and output signals originate from the avalanche multiplication process of electron-hole pairs in the sensitive area (depletion region) as a result of a light stimulus hitting its surface. Such a device can tolerate high magnetic fields up to 7 T. In addition, compared to the bulk volume of PMT devices, the compactness of the APD device allows for high packing fraction, something of critical importance for the high-resolution PET system design (Lecomte *et al* 1990, Ziegler *et al* 2001, Pichler *et al* 2001). For a brain-dedicated clinical PET/MRI system operating inside a strong magnetic field (1.5–3 T) and given the limited space inside a MRI scanner, APDs are ideal candidates for replacing PMTs.

Several groups have investigated APD-based PET detector modules with different approaches. The first design is one-to-one coupling between scintillation crystals and APDs, which is deployed in small animal PET systems (Lecomte *et al* 1990, Ziegler *et al* 2001). This design achieves high light collection efficiency, good energy resolution and good time resolution. However, such a design requires a large number of readout channels and serious challenges exist as the system scales up to a clinical system of larger field-of-view (FOV). In other words, how to use arrays of small crystal elements for high spatial resolution while reducing the number of readout channels is a fundamental challenge for the PET detector design. To address the issue, commercial PET scanners have employed position-sensitive detectors of various designs during last 30 years, including Anger-logic-type (Casey and Nutt 1986, Dahlbom and Hoffman 1988, Grazioso *et al* 2005), quadrant sharing (Wong *et al* 1994, 1999), and continuous crystal design (Joung *et al* 2002, Ling *et al* 2006). An Anger-logic-type PET detector consists of an array of scintillation crystals coupled to a matrix of photodetectors (normally  $2 \times 2$  PMTs). Each crystal has a unique light-sharing ratio among four photodetectors and their output signals are used to derive the spatial information with positioning algorithms (Casey and Nutt 1986, Dahlbom and Hoffman 1988). It is challenging to make a comprehensive comparison between different PET block detector designs. In this work, we focus on an Anger-logic-type block detector design due to its simplicity in data handling, ease of assembly/maintenance, and its widespread use in clinical PET systems (German and Hoffman 1990).

In this paper, we present a design of an Anger-logic APD-based PET block detector for a brain-dedicated PET/MRI system that uses a  $2 \times 2$  arrangement of large-area APDs. Several

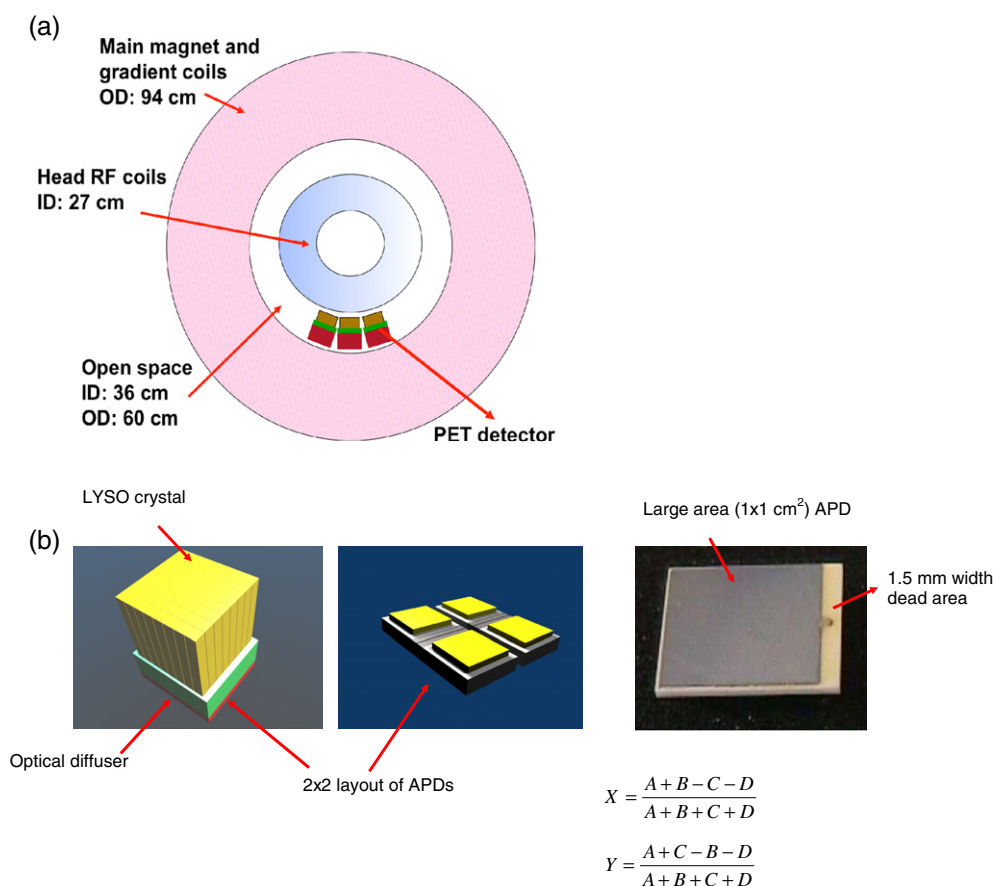


**Figure 1.** (a) Illustration of the proposed brain-dedicated PET/MRI system. Each PET block detector module consists of an LYSO scintillation crystal, an optical diffuser, a  $2 \times 2$  arrangement of large-area APDs and front-end circuits. The PET ring is to be located between the brain RF coil and the gradient coil of the MRI scanner. (b) Diagram of the proposed block detector and the  $2 \times 2$  mosaic of large-area high-gain APDs. The Anger-logic algorithm used is also shown.  $A$ ,  $B$ ,  $C$ ,  $D$  correspond to the signals from the four distinct APDs, respectively. Each APD device has an effective area of  $1.0 \times 1.0 \text{ cm}^2$  (the dead area is of  $0.5 \text{ mm}$  width on three sides and of  $1.5 \text{ mm}$  on the fourth side).

relevant issues need to be considered for such a task: (1) the crystal element width needs to be smaller ( $\sim 2.5 \text{ mm}$ ) than that in a standard clinical PET scanner ( $\sim 4\text{--}6.5 \text{ mm}$ ) in order to detect small structures of the brain while maintaining sufficient counting statistics (Humm *et al* 2003); (2) some means of light diffusion from the crystal arrays into the  $2 \times 2$  large APD arrangement is needed to be able to perform Anger logic; (3) compared to the high gain of PMTs ( $\sim 10^5\text{--}10^6$ ), APDs have a gain of  $\sim 50\text{--}1000$ , and relatively an inferior signal-to-noise ratio (SNR) due to leakage current and an increased excess noise factor. These issues might pose a limit for the block detector design.

The proposed PET detectors will be used inside a GE 3.0 T MRI scanner for brain imaging (Peng *et al* 2008). The complete PET ring is designed to operate outside RF coils but inside gradient coils, with an inner radius of approximately 36 cm (figure 1). Each PET block detector

module consists of an LYSO scintillation crystal, an optical diffuser, a  $2 \times 2$  arrangement of large-area APDs and front-end circuits. The PET ring is to be located between the brain RF coil and the gradient coil of the MRI scanner. The Anger-type logic algorithm used is also shown in figure 1. *A, B, C, D* correspond to the signals from the four distinct APDs, respectively. Each detector module requires only 4 APDs to resolve 64 relatively small size crystal elements (e.g.  $\sim 2.5$  mm resolution suitable for brain PET imaging with a multiplexing ratio of  $64/4 = 16$ ) while achieving comparable intrinsic detector performance to that achieved in clinical PET scanners for parameters such as energy resolution, time resolution and crystal identification.

The paper is organized into two parts. First, a photon transport Monte Carlo simulation tool was used to optimize the design with regard to scintillation crystal, surface treatment, optical diffuser, layout of APDs, and SNR of APD devices. Second, we present the design of a prototype detector with four different optical diffuser designs. Preliminary performance studies and results of two successful designs are reported. In addition, it is worthwhile to mention that the generalized design model developed in this work could be easily applied to other PET detector designs utilizing other photodetector technologies such as the emerging (silicon photomultiplier) SiPM (Lewellen 2008, Schaart *et al* 2009, Kolb *et al* 2010, Song *et al* 2010, Kwon *et al* 2011), since they share several similar design features including crystal array, optical diffuser, light sharing, detector dead area and SNR performance.

## 2. Methods

### 2.1. Monte Carlo simulations

All optical simulations performed in this work used DETECT2000, a Monte Carlo simulation tool for studying light transport (Knoll *et al* 1988, Moisan *et al* 1997, Rothfuss *et al* 2004). In DETECT2000, scintillation crystals, optical diffusers, and photodetectors can be specified in terms of dimensions, refractive index, attenuation mean free path, and surface treatment. A given number of optical photons are created isotropically at user-defined positions inside scintillation crystals. They will be either absorbed or scattered within the crystal bulk or optical interfaces, until they are detected eventually when they hit a photodetector's surface. The scintillation crystal employed in this work is lutetium-yttrium-oxorthosilicate (LYSO).

Parameters in the simulation are summarized in table 1. The light output profile of an incoming 511 keV photon also depends on where it deposits its energy inside a scintillation crystal, which is related to the linear attenuation coefficient of LYSO (Melcher 2000). In our simulation, 511 keV photons are generated by weighting a uniform distribution by an exponential distribution in the direction along the length of crystal elements due to the attenuation of 511 keV photons inside crystals. We limited the crystal size to 2.5–3.0 mm in order to achieve high spatial resolution and mitigate the partial volume effect. We did not study crystal width smaller than 2.5 mm as the counting statistics is a fundamental limiting factor for PET image quality and lesion detectability; reducing the crystal size by half will require eight times more counts for a PET system to maintain the same image SNR (Phelps *et al* 1986). The large-area APD employed is  $\sim 1.1 \times 1.1$  cm<sup>2</sup> (RMD Inc., Watertown, MA) and thus an  $8 \times 8$  array of 2.5 mm crystals or a  $7 \times 7$  array of 3.0 crystals seem feasible. The height (thickness) of the crystal is expected to be around 20 mm to provide sufficient stopping power for incoming 511 keV photons. Depth-of-interaction (DOI) capability will be considered in future work and is beyond the scope of this paper.

**Table 1.** Parameters used in the photon transport simulation using DETEC2000.

Scintillation material	LYSO (Lu <sub>0.6</sub> Y <sub>1.4</sub> SiO <sub>0.5</sub> : Ce)
Light yield	10 000 photons @ 511 keV
Refractive index	1.82 (LYSO crystal) 1.48 (optical diffuser made of acrylic) 1.45 (silicon)
Total visible light attenuation length	138 mm (for both LYSO crystal and the diffuser)
Linear attenuation coefficient of LYSO	0.87 cm <sup>-1</sup> @ 511 keV
Surface treatment	GROUND (roughened surface) POLISH (polished surface without reflective materials) METAL (polished surface with specular reflective materials) PAINT (polished surface with diffusive materials)

*2.1.1. Light spread function kernel.* The light spread function (LSF) kernel was studied with a single-crystal element on the top of an optical diffuser, varying the size of the crystal (both width and height), the height of the optical diffuser, and the surface treatment. Only a single large-area APD was simulated in this step. The optical diffuser and APD were considered being wide enough compared to the single crystal so that a spatial invariant LSF for a given configuration could be obtained. The light spread profile (LSP) as seen by the APD was analyzed quantitatively using formula (1). The process is illustrated in figure 2. In this step, a set of crystal and diffuser configurations were simulated (crystal width: 2.0, 2.5, 3.0, 3.5, 4.0 mm; crystal height: 5, 10, 15, 20 mm; diffuser height: ranging from 2 to 10 mm in steps of 1 mm). For each crystal and diffuser configuration, four commonly used surface treatments as defined in DETECT2000 were studied (table 1). In the simulation, surface treatments were applied only to the four side faces of each crystal, while the top surface (optical entrant face) was configured as METAL and the bottom surface (optical exit face) was configured as POLISH for all cases. The results of *A*, *B* and *C* were used as inputs for the Anger-logic positioning scheme, described in section 2.1.2:

$$\text{LSF} = Ae^{-(x/B)^2} + C. \quad (1)$$

*2.1.2. Anger-logic positioning scheme.* Assuming that all crystals within a 1D array have the same individual LSF, the Anger-logic positioning scheme was analytically modeled using the following formulae (Casey and Nutt 1986, Dahlbom and Hoffman 1988):

$$\phi_X(n) = \frac{1}{\sigma\sqrt{2\pi}} e^{-\left(\frac{n-\mu}{\sigma}\right)^2} \quad (2)$$

$$\begin{aligned} X &= (N_+ - N_-)/(N_+ + N_-), & \mu &= Np, & \sigma &= \sqrt{Npq}, \\ p &= N_+/N, & q &= 1 - p \end{aligned} \quad (3)$$

where  $\phi_x$  represents the Gaussian distribution of light output from scintillation crystals. Different from section 2.1.1, two APDs were simulated here and the light output was shared between the left APD (signal:  $N_-$ ) and the right APD (signal:  $N_+$ ).  $\mu$  and  $\sigma$  represent the

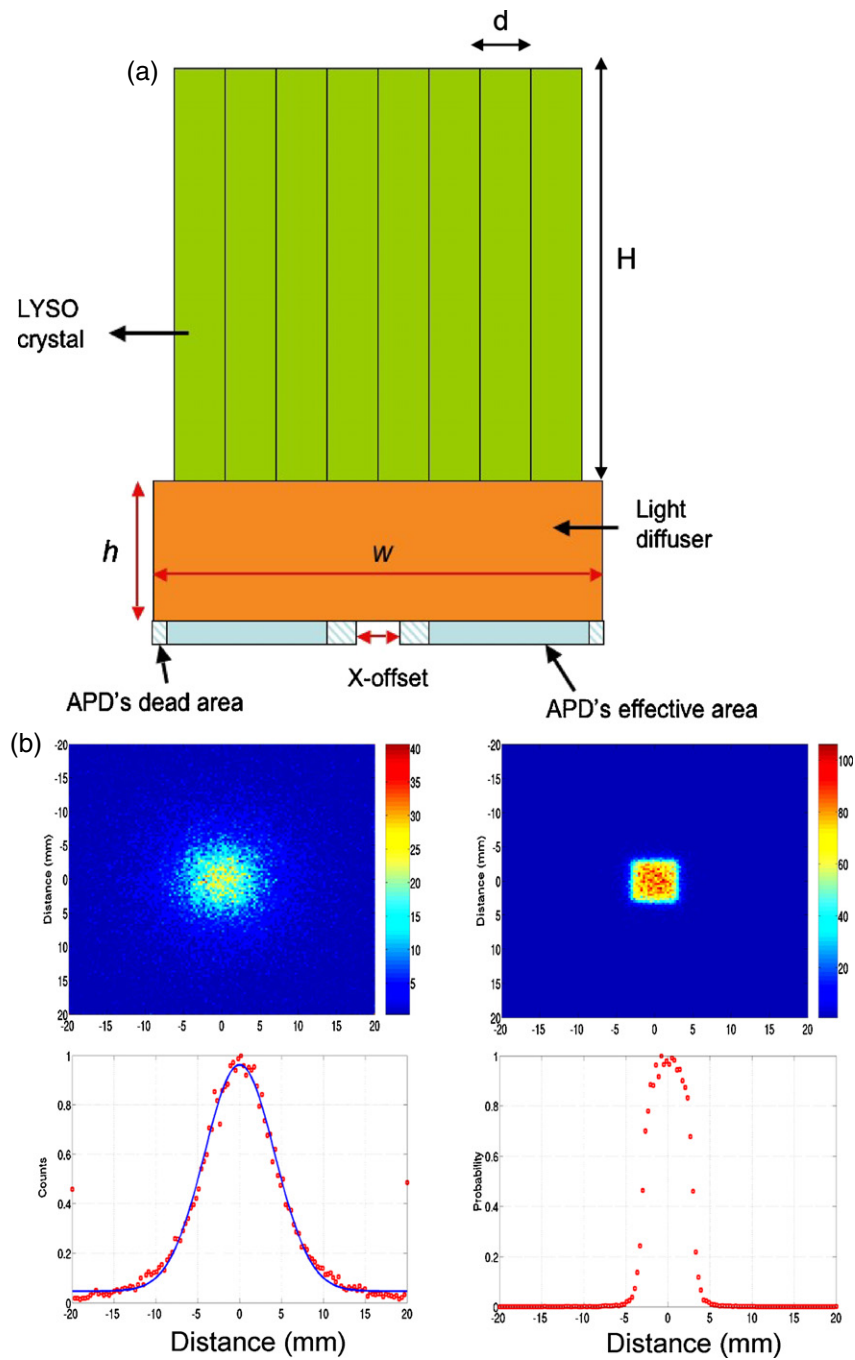


**Figure 2.** (a) Parameters modeled in the simulation:  $d$  (width of crystals),  $H$  (height of crystals),  $W$  (width of the diffuser),  $h$  (height of the diffuser). (b) Illustration of the LSP of a single LYSO crystal (2D plot and fitting) for two configurations. Left: the crystal size is  $2.5 \times 2.5 \times 20.0 \text{ mm}^3$  and the optical diffuser is 5 mm high. Right: the crystal size is  $3.0 \times 3.0 \times 20.0 \text{ mm}^3$  without optical diffuser.

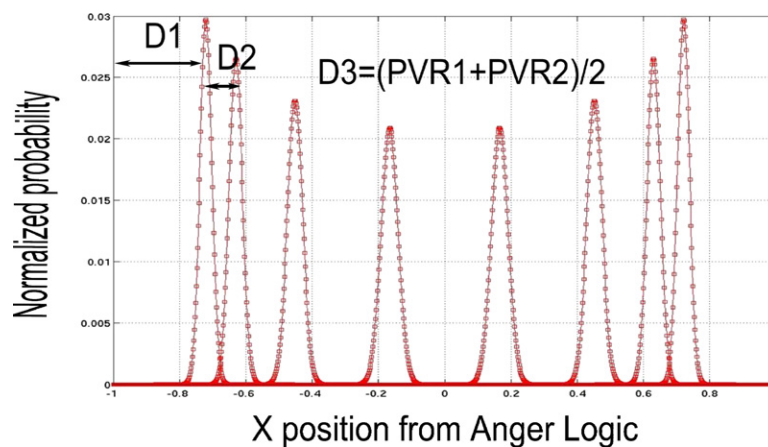


**Figure 3.** Positioning results from the analytical modeling of Anger-logic positioning for a  $1 \times 8$  crystal array ( $d$ : 2.75 mm,  $H$ : 20 mm,  $h$ : 9 mm, see figure 2).  $D_3$  is the average PVR for the two left edge crystals. The ideal positioning histogram has  $D_1$  as small as possible and  $D_2$  and  $D_3$  as large as possible.

mean (centroid) and standard deviation of each Gaussian distribution, respectively. For a given crystal pixel width, the LSF kernel obtained in section 2.1.1 was used to obtain the signals  $N_-$  and  $N_+$ , respectively.  $p$  and  $q$  refer to the possibility of light falling into each APD, which determines the light-sharing ratio.  $X$  represents the Anger-logic positioning based upon light sharing.  $N$  (the effective number of photoelectrons) was chosen to be 600. Although such estimation is an approximate representation of the true number of photoelectrons, it will not cause bias in our simulation routine as it is kept constant for all possible configurations. The  $X$  distribution (represented by  $\phi_x(n)$ ) derived from formulae (2) and (3) varies between  $-1$  and  $1$  and has the same number of peaks as the number of crystal pixels (figure 3). Three figures-of-merit were chosen ( $D_1$ ,  $D_2$  and  $D_3$ ) based on two leftmost crystals.  $D_1$  represents the distance from the edge ( $X = -1$ ) to the first peak's centroid, which indicates the spatial dynamic range of the detector positioning logic.  $D_2$  represents the distance from the first peak's centroid to the second peak's centroid, which indicates the ability to distinguish photons that interact in either of those two crystal elements.  $D_3$  is the average peak-to-valley ratio (PVR) for two peaks, which takes into account both the separation and the spread of the peaks. A good design would result in small  $D_1$  but large  $D_2$  and  $D_3$ . We studied all three parameters in the simulation but only reported  $D_3$  in this paper as it was found to be the most conclusive indicator for the optimization.

To characterize Anger-logic positioning, a set of crystal and diffuser configurations were simulated. The crystal width ranged from 2.3 to 3.0 mm with a step size of 0.1 mm. The crystal height ranged from 13 to 20 mm with a step size of 1 mm. The diffuser height ranged from 2 to 10 mm with a step size of 1 mm. For those configurations not simulated (for instance,  $2.4 \times 2.4 \times 17 \text{ mm}^3$ ), LSFs were based on linear interpolations from those LSFs studied in section 2.1.1.

**2.1.3. Effects of APD layout and edge compression.** The large-area distinct APDs to be used in the prototype have dead areas on four sides due to the manufacturing process and ceramic package (figure 1). The dead area is 0.5 mm wide on three sides and 1.5 mm wide on the

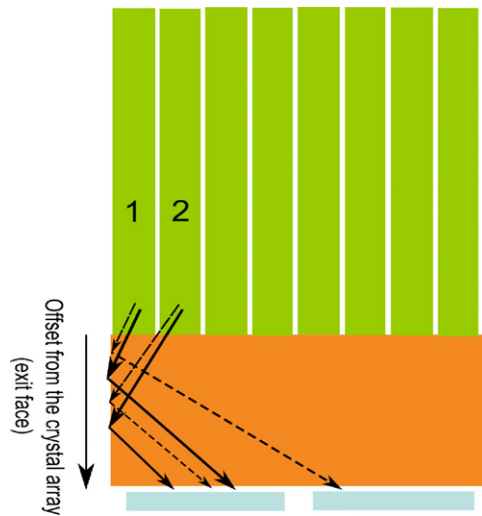


**Figure 4.** Illustration of the edge light compression effect for two crystals located at the edge of the crystal array.

fourth side (for the high-voltage connection). The  $2 \times 2$  layout of APDs strongly influences the scintillation light collection. Our rationale is that the separation between two APDs could be adjusted to improve crystal separation at the cost of some light loss. For instance, it might be preferable to arrange the APDs such that the 1.5 mm width dead regions face toward the center rather than outer peripheral regions of the scintillation crystal array. The effect of light compression at the edge is illustrated in figure 4. Recall that in the previous steps, we applied a constant LSF kernel to all crystals within a module, which is not valid for corner/edge crystals. For instance, photons exiting crystal 1 in figure 4 are more likely to hit the face of the optical diffuser side wall and will be reflected toward the APD on the opposite side. The net effect is that crystal 1 deposits more light signal on the right APD than crystal 2. As a result, the Anger-logic positioning would not work and the overlapping of two crystals would be observed in the position map (see section 3.1.2 for more details).

The task of optimizing the APD arrangement focuses on two factors: APD layout and dead area. A full LYSO array ( $8 \times 8$ ) was chosen for these simulations based on the previous optimization (crystal size:  $2.75 \times 2.75 \times 20$  mm<sup>3</sup>). For a given configuration of optical diffusers (height and width), we iterated the simulation routine searching for the optimum conditions in terms of  $2 \times 2$  APD layout. The optimization criterion is that a configuration should result in the maximum separation ( $X_2 - X_1$ ), where  $X_1$  and  $X_2$  represent the mean position (along the  $X$  direction) of the corner crystal and its adjacent crystal along the diagonal line of the detector module from Anger logic. Within each iteration, 10 000 scintillation photons were generated at a set of heights within the 20 mm length crystal element. Within each crystal in a single iteration, 200 trials (a 511 keV photon in a single trial) were simulated to estimate position fluctuations due to light propagation variations.

**2.1.4. Noise model.** The above steps did not explicitly take into account noise behaviors of photodetectors. In this step, two sources of noise were incorporated: (1) spatial noise due to Poisson statistics of light photon generation inside the LYSO crystal; (2) APD's shot noise due to leakage current and multiplication noise. A generalized model (Macovski 1983, Moszynski

*et al* 2000) was proposed to study the dependence of Anger-logic positioning on the APD SNR and the yield of light photons. First, for an incoming 511 keV photon hitting an APD, the signal and noise can be analyzed using the following formula:

$$E(S) = E(M)E(Y) \quad \text{noise}_{\text{spatial}} = \text{Var}(S) = E(M)^2\sigma_Y^2 + \sigma_M^2 E(Y)F \quad (4)$$

where  $M$  is the average gain of APD,  $Y$  is the number of e–h pairs directly generated by the incident visible photons, which is obtained from the DETECT2000 simulation output after a correction for the quantum efficiency (QE) of APD.  $S$  is the overall signal detected and  $E(S)$  represents the expected value of the signal.  $\text{noise}_{\text{spatial}}$  refers to the noise sources (signal fluctuations) resulted from scintillation light generation and APD gain fluctuation.  $F$  is the excess noise factor of the APD. The values chosen in our simulation are  $M = 1000$ ,  $\text{QE} = 60\%$ ,  $F = 2.5$ .

Second, the total noise of the detector can be separated into two components, spatial noise and shot noise, as

$$\begin{aligned} i_{\text{shot}}^2 &= 2q [I_s + I_b M^2 F(M)] B \\ \text{noise}_{\text{total}}^2 &= \text{noise}_{\text{spatial}}^2 + i_{\text{shot}}^2 \end{aligned} \quad (5)$$

where  $i_{\text{shot}}$  results from both the surface leakage current ( $I_s$ ) and the bulk leakage current ( $I_b$ ) within the APD (Moszynski *et al* 2000). However, the derivation of  $i_{\text{shot}}$  relies on the accurate measurement of several parameters, including  $I_s$ ,  $I_b$ , and bandwidth of readout electronics. Alternatively, a generalized model was developed here to investigate the SNR's effect on Anger-logic positioning. The model aims to answer two questions: (1) if a detector's SNR affects the positioning ability and the quality of flood map; (2) if we can introduce a SNR parameter to link the noise modeling here to the energy spectrum obtained later in experimental studies.

We introduced  $\text{SNR}_{\text{block}}$  as defined in formula (6), the 511 keV photopeak divided by the standard deviation of noise peak ( $i_{\text{shot}}$ ) in the energy spectrum of a given photodetector. The factor of 2 in formula (6) comes from the addition of uncorrelated noise of the four APDs, which were assumed to have the same  $i_{\text{shot}}$  value. An underlying assumption we made in formula (6) is that a corner crystal does not deposit light signals to the other three APDs except the one located right underneath the crystal itself.  $\max(A, B, C, D)$  refers to the maximum signal among the four APDs. For corner crystals,  $\max(A, B, C, D)$  is the signal of one APD collecting all the light out of the crystal, which corresponds to the signal of the 511 keV photopeak. Also note that in a detector module, the corner crystals are always subject to the effects of dead area and edge compression more significantly than other crystals. As a result,  $\text{SNR}_{\text{block}}$  for the corner crystals represents the worst SNR scenario for a block detector:

$$\text{SNR}_{\text{block}} = \frac{\max(A, B, C, D)}{2 \cdot \sigma_{\text{noisepeak}}} \quad (6)$$

For each 511 keV photon, the Anger-logic positioning was implemented in the following steps.

- (1) Signals of the four APDs were obtained from DETECT2000.  $A, B, C$  and  $D$  represent the mean signals of the four APDs (all have the Gaussian distribution). For a corner crystal,  $\max(A, B, C, D)$  is derived and it gives the signal amplitude of 511 keV photons.
- (2)  $\text{noise}_{\text{spatial}}$  of the four APDs were determined individually using formula (4).
- (3) For a given  $\text{SNR}_{\text{block}}$ , the noise ( $\sigma_{\text{noisepeak}}$ ) was first derived using formula (6) and then it was used to estimate  $i_{\text{shot}}$  individually for four APDs.

Anger-logic positioning without and with noise was studied for only a  $4 \times 4$  LYSO portion of the  $8 \times 8$  LYSO crystal array (one quadrant of the  $8 \times 8$  array) due to symmetry. Three  $\text{SNR}_{\text{block}}$  values (50, 30, 15) and associated flood maps were studied. When noise is



**Figure 5.** Left: the block detector prototype comprising the LYSO array, the optical diffuser (design II), the  $2 \times 2$  layout of APDs and custom readout electronics. Middle: the detector prototype test board. The APD region with largest dead areas (1.5 mm width) is located in the central region rather than the edge of the array. Right: a slotted optical diffuser assembled from nine separate pieces.

present, two noise sources ( $\text{noise}_{\text{spatial}}$  and  $i_{\text{shot}}$ , both assuming Gaussian noise) were added into raw signals from DETECT2000 simulations and then the Anger-logic positioning was implemented. Each trial corresponds to a 511 keV event and generates a point in the flood map. In total, 600 trials were made.

## 2.2. Experimental studies

**2.2.1. Scintillation crystal array and  $2 \times 2$  layout of large-area APDs.** An  $8 \times 8$  LYSO scintillation crystal with crystal element dimensions of  $2.75 \times 3.00 \times 20.0 \text{ mm}^3$  was built (figure 5). Each crystal pixel was optically isolated from other crystals by high reflection coefficient (98% RC) specular reflective materials (VM2000 tape, thickness  $75 \mu\text{m}$ , 3M Company, USA). The APDs were provided by RMD (Watertown, MA, USA). The asymmetry of APD dead area (see figure 1) is the reason why the crystal width is not symmetric ( $2.75 \text{ mm} \times 3.00 \text{ mm}$ ). The capacitance of each APD is  $0.7 \text{ pf mm}^{-2}$ . The scintillation crystal array, optical diffuser and  $2 \times 2$  arrangement of large-area APDs were coupled with optical grease BC630 (Saint Gobain, USA).

**2.2.2. Optical diffuser designs.** Based on the simulation, four designs of optical diffuser were studied (figure 6). Optical diffusers were made of acrylic plastic materials and all surfaces were chemically polished. The cross-sectional area of each diffuser matches the total size of the crystal array except in design IV. Diffuser design I consists of a whole piece with the height varying between 3 and 10 mm. Four sides of the diffuser are coated with the VM2000 tape. For the other three designs, only the one with 9 mm height was tested based on the results from design I.

Diffuser design II is a dual layer design. The top layer (2 mm) of the diffuser is coated by an optical absorption material (electrical black tape) which is estimated to have  $\sim 95\%$  absorption efficiency. The bottom layer (7 mm) is covered with VM2000 tape. This design is expected to mitigate the edge light compression effect (a result of excessive reflection at the edges) and restore the separation between crystals. The drawback associated with this design is that light loss occurs due to the light absorption in the top layer, which will degrade the SNR of the APD.

However, as to be seen in section 3, design II fails to resolve all crystals in the block. Two other diffuser designs were developed. Designs III and IV are both slotted designs that involve the assembly of nine pieces. VM2000 tape is inserted in between the pieces as well as the

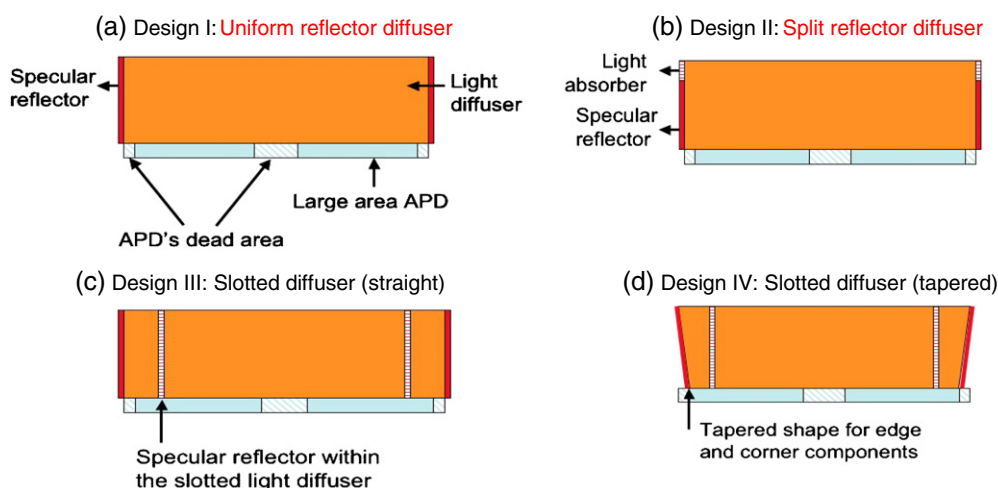


**Figure 6.** Schematic design of four optical diffuser designs tested. In design I, four sides are wrapped with specular reflectors. In design II, the top layer of 2 mm height is wrapped with black tape, while the remaining 7 mm is wrapped with specular reflector. In design III, separate pieces are made and specular reflectors are inserted in between. In design IV, the same slotted design as III is used but has a tapered shape (tapering angle  $\sim 10^\circ$ ) for edge pieces in order to overcome the light loss at the dead perimeters of APDs.

outer faces of assembled blocks. The rationale here is that by introducing an optical barrier between corner/edge crystals and other crystals, light photons from corner/edge crystals are prevented from arriving at the APDs on the opposite side. As a result, the edge compression can be overcome without light loss. However, this would make the optical diffuser assembly more complex and slightly increase the detector's cost. The difference between designs III and IV is that in the latter one, eight pieces (except the central piece) are configured in a tapered shape aiming to overcome light loss occurring at the outmost dead areas of the block.

**2.2.3. Characterization of individual APDs and the block detector.** The data acquisition system is briefly described here. Charge-sensitive preamplifiers and shaping amplifiers (time constant:  $\sim 100$  ns) were used. The output signals were simultaneously processed with commercially available data acquisition electronics (PCI-6143, National Instruments, USA). Peak sensing was triggered by an external logic signal generated by an ORTEC 935 constant-fraction-discriminator (CFD) module. Signals of four channels were saved to obtain energy spectra and Anger-logic positioning.

For the coincident timing measurement, a Hamamatsu fast PMT R9779-20 coupled to a  $4.0 \times 4.0 \times 20.0$  mm<sup>3</sup> LYSO crystal was configured in coincidence to the block detector. The PMT was biased at 1750 V and its output was directly connected to the ORTEC 935 CFD without any filtering. For the block detector, the four APD signals were first summed to a single channel using a summing circuit and then connected to an ORTEC 474 fast filter amplifier. The fast output was then fed into the ORTEC 935 CFD to pick off the timing. Two CFD outputs were finally connected to an ORTEC 567 time-to-amplitude converter (TAC) to get the time spectrum. A  $10 \mu\text{Ci } ^{22}\text{Na}$  sealed source was located between and equidistant to the two detectors. The distance between the faces of two detectors was 15 cm.

Prior to evaluating the block detector, the energy spectrum and time spectrum were obtained for a single APD with a single LYSO crystal of size  $3.0 \times 3.0 \times 20.0$  mm<sup>3</sup>. Its

performance was optimized as a function of high voltage in terms of energy resolution. Once the performance of four APDs was optimized individually, we evaluated the block detector with the four optical diffuser designs. For the two designs that are able to resolve all 64 crystals (designs III and IV), the crystal flood maps were segmented using a k-mean clustering and voronoi algorithm (MATLAB, MathWorks, Inc., USA). Finally, we analyzed the block detector's performance including energy resolution, time resolution,  $\text{SNR}_{\text{block}}$ , uniformity, and PVR.

### 3. Results

#### 3.1. Simulation study

**3.1.1. Crystal array optimization.** For two chosen crystal element configurations ( $2.5 \times 2.5 \times 20.0 \text{ mm}^3$  and  $3.0 \times 3.0 \times 20.0 \text{ mm}^3$ ), the LSFs are shown in figure 2(b). The results indicate the presence of LSF dependence on the crystal size and the optical diffuser's height.  $D_3$  values as a function of the diffuser's height are shown in figure 7(a) for four different surface treatments (crystal element dimensions:  $2.5 \times 2.5 \times 20.0 \text{ mm}^3$ ). Larger  $D_3$  values are achieved when the diffuser has a height around 6–9 mm (METAL, crystal covered by specular reflectors) and 7–10 mm (crystal covered by diffusive reflectors). This indicates that the usage of reflectors helps confine the light spreading and maintain the original spatial information of crystals, as previously found in MicroPET detector designs (Chatziioannou *et al* 2001). The specular reflector is preferred over diffusive reflectors as it shows approximately 1.5 times higher light output in our simulation, which is also consistent with the previous study with a similar crystal configuration ( $2.0 \times 2.0 \times 10 \text{ mm}^3$ ) (Heinrichs *et al* 2002). For crystal element configurations of  $2.0 \times 2.0 \times 20.0 \text{ mm}^3$  and  $3.0 \times 3.0 \times 20.0 \text{ mm}^3$ , a similar pattern is found that large  $D_3$  occurs when the diffuser is of 6–9 mm height.

The 2D contour plot of  $D_3$  as a function of the crystal's width and height is shown in figure 7(b) with an 8 mm high optical diffuser. It is observed that for a given crystal's width (ranging from 2.3 to 3.0 mm), increasing the crystal's height from 13 to 20 mm results in the decrease of  $D_3$  since the light spread shrinks when the crystal aspect ratio (width over height) becomes smaller, though the crystal will have more stopping power for 511 keV photons. On the other hand, for a given crystal height, increasing the crystal width from 2.3 to 3.0 mm yields an initial increase of  $D_3$  followed by a decrease. These results imply that there exists an optimum crystal/diffuser configuration for the largest  $D_3$  (i.e. best crystal separation) when other effects such as detector dead area and edge light compression are not considered. The crystal configuration of  $2.75 \times 2.75 \times 20.0 \text{ mm}^3$  and the surface treatment of METAL (specular reflector) were chosen for the studies presented in the following sub-sections.

**3.1.2. APD layout and optical diffuser optimization.** Impact of APD layout and edge compression on crystal separation is illustrated in figure 8(a). For a given diffuser's configuration (width: 24.0 mm, height: 9 mm), the dotted region indicates that the maximum ( $X_2 - X_1$ ) (refer to section 3.1.3) is achieved when offset\_X is  $\sim 1.6$  mm and offset\_Y is  $\sim 1.8$  mm. Note that the width of the optical diffuser is larger than the width of the full crystal array ( $2.75 \text{ mm/crystal} \times 8 \text{ crystals} = 22.0 \text{ mm}$ ). For all possible diffuser configurations, such 2D plots and the maximum ( $X_2 - X_1$ ) values are obtained. The question arises here why offset\_X has the range of  $-1.5$ – $2$  mm and offset\_Y has the range of  $0$ – $2$  mm. This is because an APD has asymmetric dead area (i.e. one edge of 1.5 mm width along the X direction and of 0.5 mm width along the other three edges, see figure 1). Such a concept is further explained in figure 8(b).

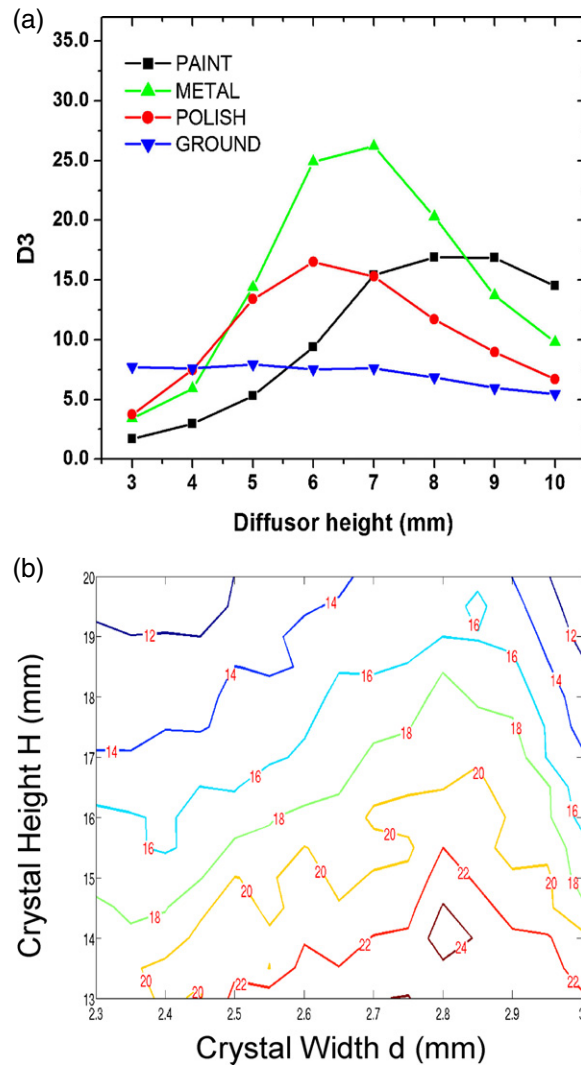


**Figure 7.** (a)  $D_3$  (see figure 3) as a function of surface treatment and optical diffuser height (crystal element dimensions:  $2.5 \times 2.5 \times 20.0 \text{ mm}^3$ ). Large  $D_3$  appears when the height of the optical diffuser varies between 6 and 9 mm. (b) The 2D contour plot of  $D_3$  as a function of  $d$  and  $H$  (see figure 2; optical diffuser height: 8 mm). The LSFs for those scenarios that are not simulated in DETECT2000 are based on linear interpolation.

In our simulation model, a positive  $\text{offset}_X$  implies that the 1.5 mm dead area side of each APD is facing toward the middle APDs (see figure 5 middle) and an additional separation ( $\text{offset}_X$ ) is applied; while a negative  $\text{offset}_X$  implies that the 1.5 mm dead area of each APD is located in the outer regions of two APDs with an additional separation applied ( $2 \times 1.5 \text{ mm} + \text{offset}_X - 2 \times 0.5 \text{ mm}$  for each APD; 0.5 mm is the dead area on the other side of APD along the  $X$  direction). However,  $\text{offset}_Y$  is defined differently and it ranges only from zero to 2 mm, because the APD dead area is symmetric along the  $Y$  direction (0.5 mm for both sides). Assuming a square shape detector, it requires an extra 1.0 mm (difference between 1.5 and 0.5 mm) to be introduced for each APD along the  $Y$  direction. Therefore,  $\text{offset}_Y$  represents that 0.5 mm dead area of each APD located in between two APDs

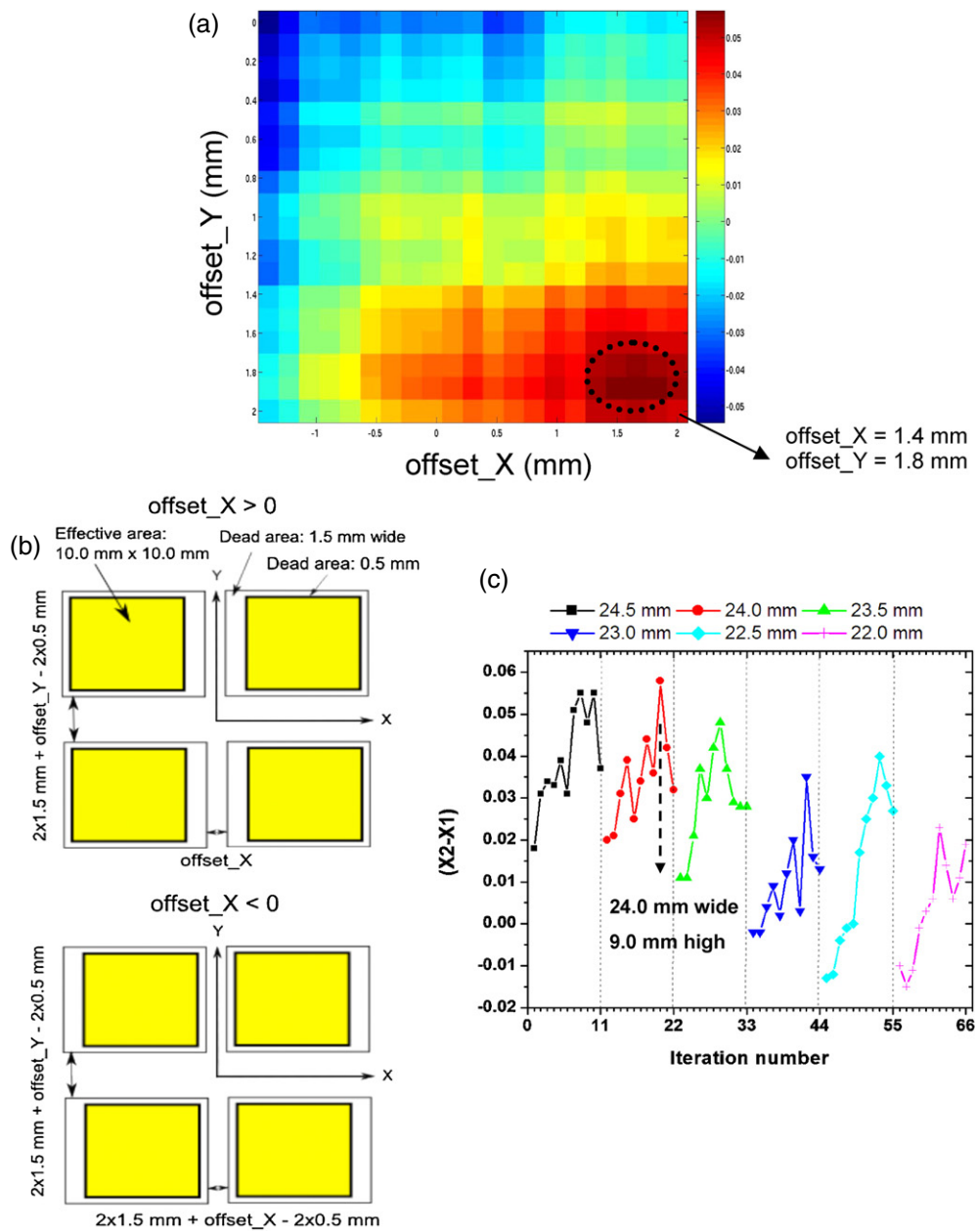


**Figure 8.** (a) Maximizing  $(X_2 - X_1)$  (the separation between the corner crystal and its adjacent crystal) as a function of  $\text{offset}_X$  and  $\text{offset}_Y$ , for a given configuration (crystal size:  $2.75 \times 2.75 \times 20.0$  mm<sup>3</sup>, optical diffuser: 24.0 mm width and 9.0 mm high). (b) Illustration of APD layout adjustment through  $\text{offset}_X$  and  $\text{offset}_Y$ . (c) Maximum  $(X_2 - X_1)$  values for various diffuser configurations (different colors indicate different diffuser widths). For instance, iteration number [1–11] (leftmost 11 data points) corresponds to an increase of diffuser height from 5 to 10 mm for a diffuser width of 24.5 mm.

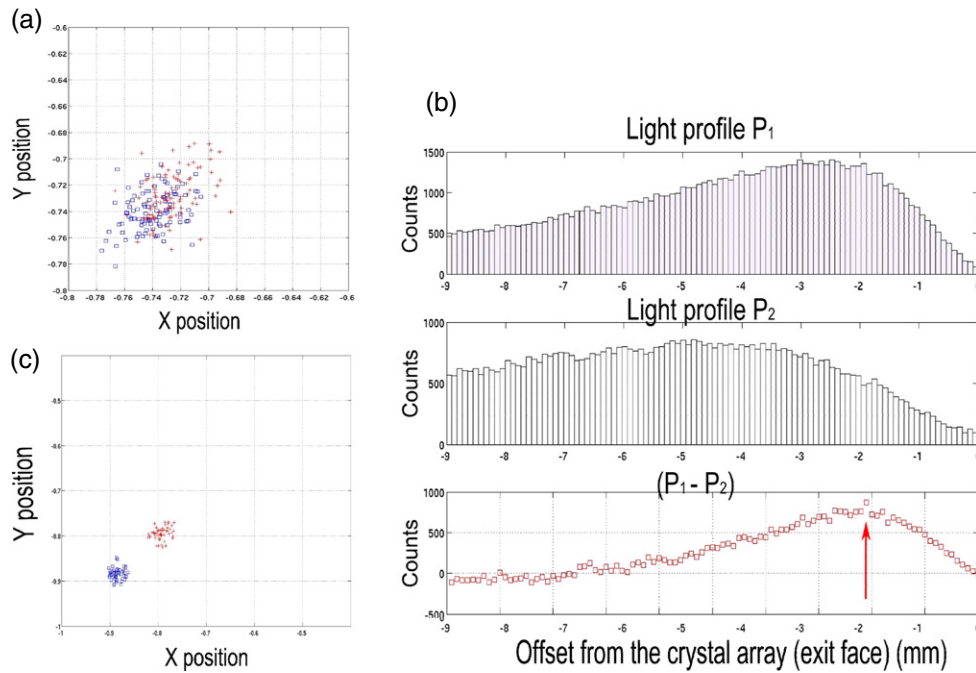


**Figure 9.** (a) Position map under the optimum diffuser configuration (width: 24.0 mm and height: 9 mm) found in figure 8(c) (only 50 out of 200 simulated 511 keV photons are shown). (b) The scintillation LSPs ( $P_1$  and  $P_2$ ) as a function of the offset from the crystal array, as well as the difference ( $P_1 - P_2$ ). The offset here refers to the depth into the diffuser measured from its entrance window, which decreases from zero to negative values. It is expected that the edge light compression effect could be mitigated by attenuating light signals located between 0 and  $-2$  mm indicated by the arrow with an absorber. (c) Position map with the dual layer diffuser design (design II shown in figure 6(b)).

(1.0 mm dead area in total) and an additional separation ( $2 \times 1.5 \text{ mm} + \text{offset}_Y - 1.0 \text{ mm}$ ) are applied.

The optimum ( $X_2 - X_1$ ) values for all possible diffuser configurations are shown in figure 8(c). Each data point is derived from the optimization routine illustrated in figure 8(a) (the maximum value within the 2D plot). For instance, ( $X_2 - X_1$ ) values (11 leftmost points) are presented in that figure for the case when the optical diffuser has 24.5 mm width and its thickness varies from 5 to 10 mm in a step size of 0.5 mm. Two characteristics are observed: first, for all scenarios, the largest ( $X_2 - X_1$ ) occurs when the optical diffuser has a height of around 8–9 mm. Second, as the width of the diffuser increases from 22.0 (11 rightmost points) to 24.5 mm (11 leftmost points), the maximum ( $X_2 - X_1$ ) slightly increases from 0.02 to 0.05. It should be pointed out that such an improvement is very marginal when compared to the dynamic range (from  $-1$  to  $1$ ) available to Anger-logic positioning. Also note that a PET system cannot afford the separation between two APDs (i.e.  $X$  offset and  $Y$  offset) in a detector too large, as it will result in poor packing fraction.

Under the diffuser configuration where the maximum ( $X_2 - X_1$ ) of  $\sim 0.06$  is achieved (24.0 mm width and 9 mm thickness), the position map of two crystals is shown in figure 9(a). Significant overlap between the corresponding crystal peaks indicates that the light sharing is not sufficient to resolve those two crystals. Therefore, no more attempts to increase ( $X_2 - X_1$ ) through adjusting APD layout were made. In the following experimental study, the total dead

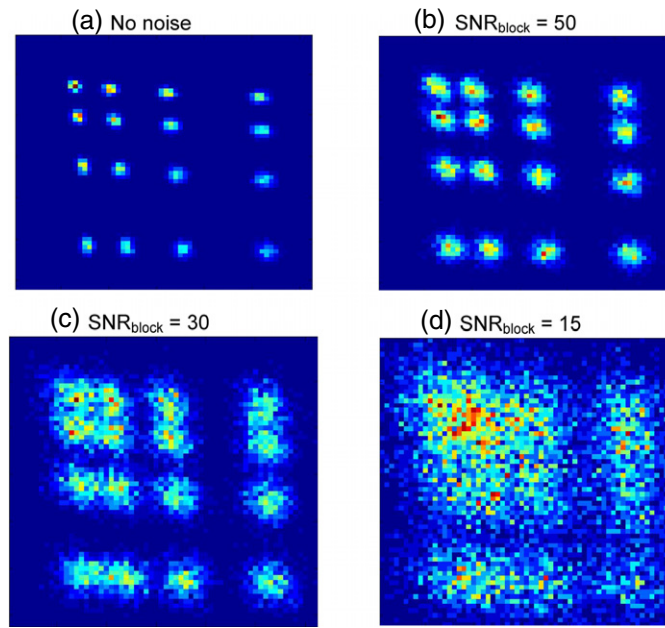


**Figure 10.** Simulated flood histograms of one quadrant of detector comprising an  $8 \times 8$  LYSO crystal array coupled to a  $2 \times 2$  layout of large-area APDs as a function of  $\text{SNR}_{\text{block}}$  (see formula (6)). The dimensions of each array crystal element are  $2.75 \times 2.75 \times 20.0 \text{ mm}^3$  and those of the optical diffuser  $24.0 \times 24.0 \times 9.0 \text{ mm}^3$ . Only one quadrant for the  $8 \times 8$  array was simulated due to the symmetry. Significant degradation of the flood histogram is observed as  $\text{SNR}_{\text{block}}$  decreases. (a) No noise, (b)  $\text{SNR}_{\text{block}} = 50$ , (c)  $\text{SNR}_{\text{block}} = 30$ , (d)  $\text{SNR}_{\text{block}} = 15$ .

area in between two APDs was fixed at 3.0 mm along the  $X$  direction and 1.0 mm along the  $Y$  direction.

The edge compression effect was investigated and the results are presented in figure 9(b). The LSPs for light created near the diffuser's side wall are shown for two crystals ( $P_1$  and  $P_2$ ). All visible photons interacting with the specified side wall of the diffuser were recorded and their position information was used to plot histograms. The offset refers to the depth into the diffuser measured from its entrance window. The locations of two crystals with respect to the side wall of the optical diffuser have been illustrated in figure 4. From 0 to  $-6$  mm,  $P_1$  has higher intensity than  $P_2$  which indicates that more visible photons are hitting the region between 0 and  $-6$  mm. Those scintillation light photons would be reflected and are more likely to hit the APD on the opposite side, as predicted in figure 4. As a result, crystal 1 deposits more light signal in the right APD than crystal 2 and the Anger-logic positioning would result in the overlapping effect shown in figure 9(a). Furthermore,  $(P_1 - P_2)$  reaches a maximum at an offset of  $-2$  mm indicated by the arrow. If photons interacting with the top layer (0 to  $-2$  mm) can be effectively absorbed, the edge compression is expected to be suppressed while the light loss can be kept to a minimum. The updated flood map based upon such a concept (design II in section 3.2.2) is shown in figure 9(c) where two edge crystals are clearly separated. However, such a design, which worked in simulation, failed to produce well-separated edge crystals in actual experiments.

**3.1.3. Noise model.** The results of noise modeling are shown in figure 10 based on diffuser design II. The crystal flood histogram is more blurred and the separation degrades since  $\text{SNR}_{\text{block}}$  decreases. When the  $\text{SNR}_{\text{block}}$  is 30, crystals are still resolvable by observation.

However, when the  $\text{SNR}_{\text{block}}$  is 15, the edge crystals are no longer resolvable. From section 3.2.1, we predict that the proposed LYSO+ large-area APD block assembly would achieve a  $\text{SNR}_{\text{block}}$  of  $\sim 21.0$ , where the voltage signal corresponding to the 511 keV photopeak was measured to be 2.8 V and the voltage signal corresponding to the standard deviation of the noise peak was measured to be 0.067 V.

For designs III and IV, we did not implement noise analysis due to complexities in modeling slotted diffusers. However, as the slotted designs could address edge LSP compression without causing light loss (i.e. light sharing would remain approximately uniform even at the edge), we predict that the SNR in designs III and IV will be slightly higher than for design II. For instance, if the light loss occurring at the top layer (2 mm) is 20% of the total light output for a corner crystal, the SNR of designs III and IV would be  $(5/4) \times 21.0 = 26.25$ , which would result in a similar crystal flood histogram as shown in figure 10(c). The factor (5/4) is estimated from figure 9(b), where the light photons absorbed at the sides between 0 and  $-2$  mm account for approximately one-fifth of the total light photons collected, which ultimately results in 20% loss of light in design II.

### 3.2. Experimental study

**3.2.1. Single-APD characterization.** The energy spectrum of a single-APD device coupled to a single crystal located at the central region of the APD is shown in figure 11. The energy resolution is  $11.5 \pm 0.4\%$  FWHM for 511 keV photons. The optimum energy resolution (reported here) is achieved at a bias of 1710 V and shaping time of 100 ns. Optimizing the energy resolution for individual devices leads to higher  $\text{SNR}_{\text{block}}$ , as defined by formula (6). Four APDs were then biased at 1710 V (gain variation among APDs was measured to be less than 5%) and amplitudes of each in response to 511 keV photons were calibrated to the same amplitude by adjusting the amplifier settings. The coincidence time spectrum with a single LYSO crystal coupled to a large-area APD detector in coincidence with the LYSO-PMT detector is shown in figure 11. The time resolution is  $1.96 \pm 0.10$  ns, which is mainly limited by the decay time of LYSO ( $\sim 30$  ns) and the internal capacitance of the large-area APD.

**3.2.2. Block detector characterization.** Flood histograms with four optical diffuser designs are shown in figure 12. For designs I and II, all 64 crystals are not fully resolved for either 511 keV and 1.275 MeV photons shown in figures 12(a) and (b). The crystal separation for 1.275 MeV is better than that of 511 keV photons, due to higher light yield of LYSO crystals under the irradiation by higher energy photons. In addition, we compare the flood maps with diffusers of height varying from 3 to 10 mm for design I. The 9 mm height provides the best result in terms of the dynamic range of the flood histogram even though it could not resolve all crystals. This is in good agreement with the simulation results shown in figures 7(a) and 8(c).

For designs III and IV, all 64 crystals are fully resolved for 511 keV photons, as seen in figures 12(c) and (d). The two flood histograms (designs III and IV) both have a dynamic range of  $[-0.6 \ 0.6]$  along the  $X$  direction (horizontal direction, corresponding to 3.0 mm crystal width) and of  $[-0.8 \ 0.8]$  along the  $Y$  direction (vertical direction, corresponding to 2.75 mm crystal width). The two flood histograms were segmented into 64 regions-of-interest (ROIs) and each ROI was stored into a look up table. Voronoi plots were laid upon the raw flood images to show crystal segmentation. A corner crystal in figure 12(d) (top left corner) was chosen for the SNR analysis. The energy spectra of two APDs (APD A and APD C) are shown, respectively. For the chosen crystal, the maximum signal is found in APD A and the noise signal is obtained from APD C. The SNR is 30.9 for design IV and 31.2 for design III,

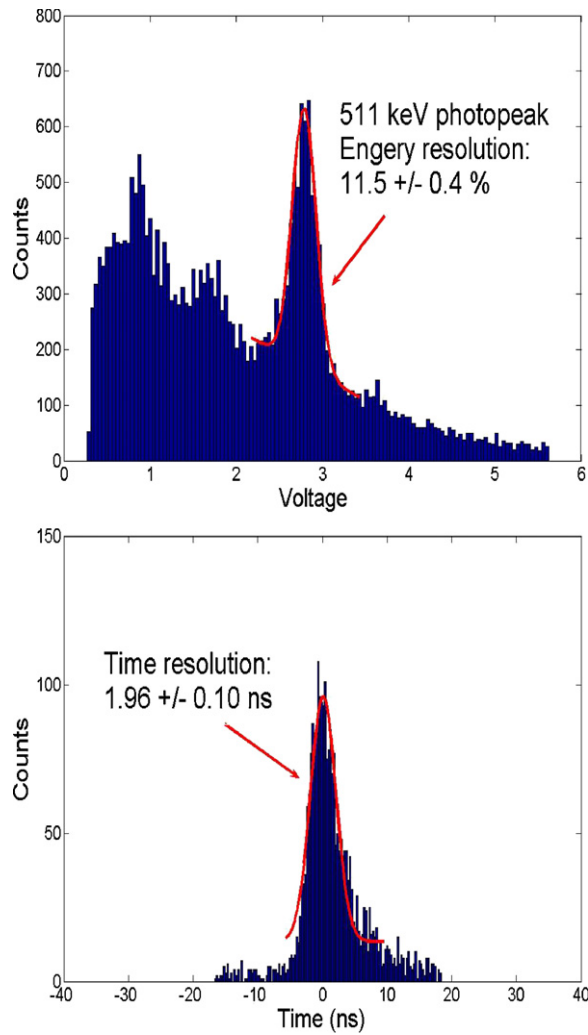


**Figure 11.** Experimentally measured energy and time spectrum for a single LYSO crystal element (dimensions:  $3.0 \times 3.0 \times 20.0 \text{ mm}^2$ ) coupled to a large-area APD (irradiated by a  $^{22}\text{Na}$  source). The time spectrum was measured in a coincidence mode with a PMT (Hamamatsu R9779-20) coupled to a  $4.0 \times 4.0 \times 20.0 \text{ mm}^3$  LYSO crystal.

which agree reasonably well with the simulation results in figure 10. For diffuser designs I and II, it is difficult to segment corner crystals even in the flood images for 1.275 MeV photons due to the side reflections resulting in crystal overlapping. Therefore, the four corner crystals on the top-left corner of the flood image were grouped together for the SNR analysis. The SNRs for designs I and II are 26.2 and 28.4 (for 1.275 MeV photons), respectively. The derived SNRs might be an underestimation of true SNRs, as the underlying assumption of formula (6) is no longer valid as we cannot isolate a corner crystal clearly from its adjacent ones. In other words, the next three crystals away from the corner will deposit some portion of signals to the other three APDs ( $B$ ,  $C$  and  $D$ ) and, thus,  $\max(A, B, C, D)$  in formula (6) will be underestimated and is lower than the amplitude of 511 keV photopeak. Translating from 1.275 MeV photons to 511 keV photons, the SNR would scale down by a factor of  $\sim 2.5$  (ignoring the energy nonlinearity of LYSO) and to 10.5 (design I) and 11.4 (design II),

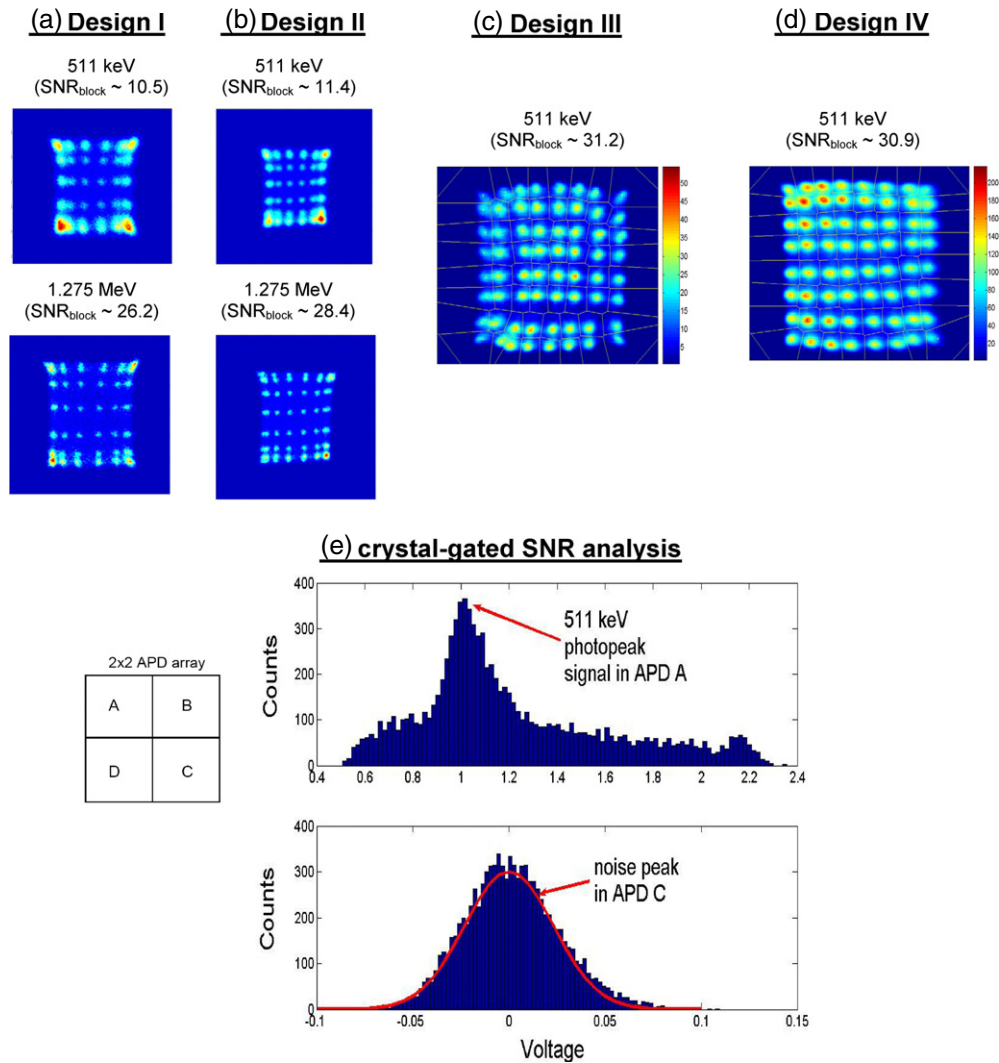


**Figure 12.** Measured flood histograms for diffuser design I (a), design II (b), design III (c) and design IV (d) (see figure 6), and plots used for the SNR analysis (e). Both horizontal and vertical scales in all flood maps range from  $-1$  to  $1$ . In (e), the energy spectra gated for the corner crystal (first row, first column, right on the top of APD A) are shown. The 511 keV photopeak measured in the APD A and the sigma of the noise peak in the APD C were used to characterize  $\text{SNR}_{\text{block}}$ . As mentioned in the definition of formula (6), the assumption we made here is that by optimizing the optical diffuser design, the selected crystal at the corner deposits nearly all of its light output in the APD A and does not deposit its light output in the APD C. The noise peak in the energy spectrum of the APD C is purely due to its leakage current ( $i_{\text{shot}}$ ).

respectively. Under such a low SNR, poor crystal separation in flood histograms is expected according to the simulation results presented in figure 10.

The results are summarized in table 2, with both the position gating and energy gating (twice FWHM centered on the 511 keV photopeak) applied. Overall, the  $2 \times 2$  large-area APD block detector exhibits good uniformity among 64 crystals. In table 2, relative gain refers to the gain (i.e. the photopeak position) of a single crystal with respect to the highest gain among 64 crystals. Relative sensitivity refers to the photon sensitivity (i.e. the counts

**Table 2.** Summary of measured results for designs III and IV.

		Design III	Design IV
Relative sensitivity	Maximum	1.00	1.00
	Minimum	0.50	0.56
	Mean	0.78	0.87
Relative gain	Maximum	1.00	1.00
	Minimum	0.65	0.70
	Mean	0.86	0.89
Energy resolution FWHM (%)	Maximum	$17.3 \pm 0.4$	$23.8 \pm 1.0$
	Minimum	$11.3 \pm 0.3$	$14.9 \pm 0.6$
	Mean	$13.8 \pm 0.4$	$17.9 \pm 0.6$
Coincidence time resolution FWHM (ns)	Center crystal	$4.85 \pm 0.04$	$5.01 \pm 0.06$
	Edge crystal	$5.17 \pm 0.06$	$5.17 \pm 0.08$
	Corner crystal	$5.18 \pm 0.07$	$5.18 \pm 0.08$

under the 511 keV photopeak in the energy spectrum) of a single crystal with respect to the highest count among 64 crystals. A slight improvement of energy resolution in design III compared to design IV is observed. For both designs, the edge and corner crystals exhibit lower photon sensitivity, lower gain and poorer energy resolution, compared to crystals in the central region. The global energy spectra of designs III and IV after gain normalization are shown in figure 13. The energy resolution FWHM for 511 keV photons is  $13.4 \pm 0.4\%$  (design III) and  $16.5 \pm 0.4\%$  (design IV), respectively. Both are inferior to the energy resolution of a single-APD device (figure 11).

The coincidence time spectra of designs III and IV were studied for three crystals. Based on the flood maps in figures 12(c) and (d), a corner crystal located on the top row and the left column, an edge crystal (top row and left column), and a center crystal (fourth row and fourth column) were chosen. In figure 13, a typical time spectrum is shown for the chosen center crystal for design III. The results are summarized in table 2. Slightly improved time resolution is observed for the center crystal, compared to the edge and corner crystals in both designs. No significant difference is observed between two designs.

For a selected central row (fifth row) and column (fifth column), two profiles are shown in figure 13(c) and the average and standard deviation of PVR results are listed to characterize the crystal resolving ability. For each peak, the PVR was derived by first calculating the ratio of peak amplitude over amplitudes of two adjacent valleys and then taking the average. The average PVR for design III is  $2.65 \pm 1.13$  and  $4.20 \pm 1.92$ , respectively. The average PVR for design IV is  $2.52 \pm 0.60$  and  $3.52 \pm 0.90$ , respectively.

#### 4. Discussion

We systematically optimized the design for the proposed large-area APD-based block detector with a simulation tool. Based upon simulation results, a block detector prototype was built and four designs of optical diffuser were tested. In two designs using slotted optical diffusers, the detector prototype exhibits satisfactory performance, in terms of energy resolution, time resolution, uniformity and crystal separation observed in a flood histogram. We believe that such results would enable a brain-dedicated PET/MRI to achieve even better performance compared to currently available whole-body PET systems, and thus, the design could be appropriate for a clinical PET/CT system.

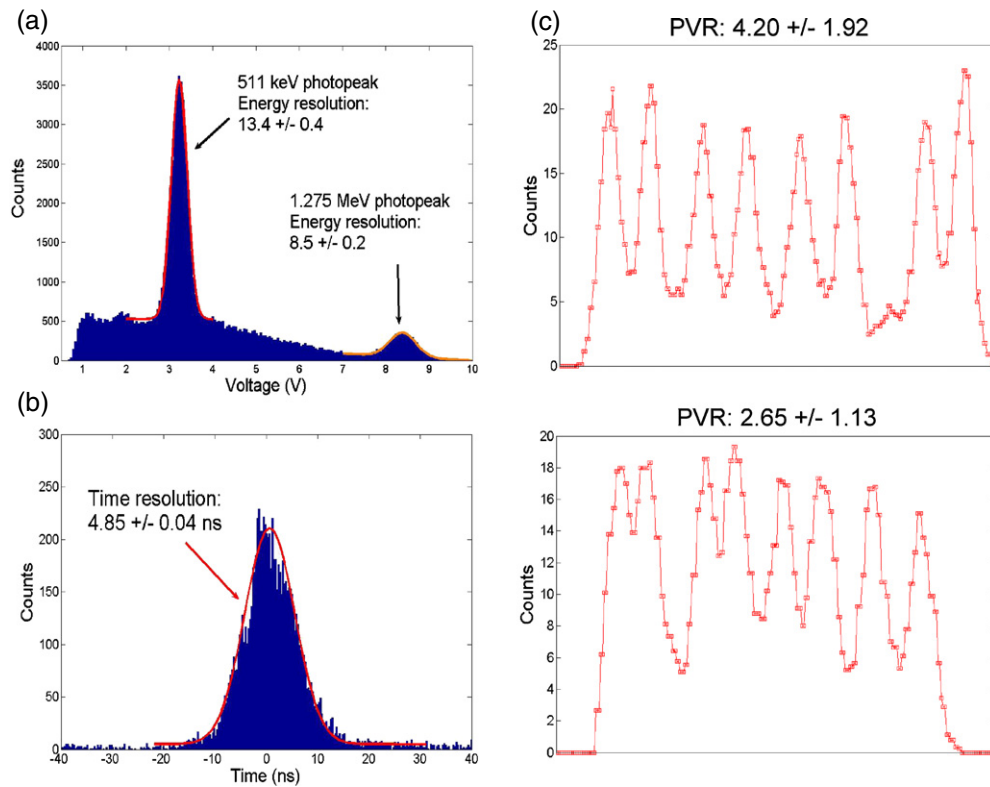


**Figure 13.** (a) Measured global energy spectrum over all 64 crystals after gain calibration. (b) Measured coincidence time spectrum between a center crystal (located on the fourth row and fourth column in the flood histogram, figure 12(c)) of the  $2 \times 2$  APD array block in reference to a LYSO-PMT detector. (c) 1D profiles through the measured flood histograms in figure 12(c) corresponding to the fifth column (top) and fifth row (bottom).

#### 4.1. Simulation study

For a block detector based upon light sharing but without light crosstalk between crystals, Anger-logic positioning relies mainly on the LSF kernel and the associated light-sharing ratio between two APDs. LSF is dependent on the crystal dimension (both width and height, described by the aspect ratio) and on the height (thickness) of the optical diffuser. In general, when crystals have larger aspect ratio and the optical diffuser is thicker, the LSF gets broader and there is more light output. Furthermore, with a thick optical diffuser in place, the light-sharing ratio depends strongly on the light spread within the diffuser as supported by figure 7(a). Second, the LSF is also dependent on the light-spread within crystals as indicated in figure 7(b).

Figure 7 also implies that for the proposed block detector requiring a thick optical diffuser, the light sharing contributed from the light spread within the optical diffuser is more dominant than from the light spread within a crystal pixel. There is an optimum configuration of the crystal/diffuser which leads to the best edge crystal separation. With a thinner optical diffuser or a smaller crystal width, two edge crystals are not able to deliver enough light to the opposite photodetector (i.e. under-spread of light); while with a thicker optical diffuser or a larger crystal width, the light sharing overrides the original spatial information of two edge crystals

and thus causes the  $D_3$  to decrease (i.e. over-spread of light). These two scenarios should be avoided in the block detector design.

The light sharing is also dependent on the layout of the large-area APDs due to edge light compression and dead areas. The edge compression is most significant for edge/corner crystals and could be addressed by utilizing either a dual layer diffuser or a slotted diffuser. Both of them essentially introduce an optical barrier within the diffuser and thus modify the light-sharing ratio for crystals. Simulation results show that by solely optimizing the APD's layout and the dimensions of the diffuser, good crystal separation could not be achieved in figures 8 and 9(a), while the dual layer diffuser significantly suppresses the edge compression and enables the two edge crystals to be resolved as shown in figure 9(c).

A weak dependence of crystal separation on the optical diffuser's width is observed in figure 8(c). Additional separation between peaks of edge crystals can be introduced by actively separating APDs. In other words, the dead area of APDs is not necessarily a limitation for resolving edge crystals in the proposed large-area APD-based block detector design. We could extend the diffuser slightly beyond the edge of the crystal array to improve the crystal separation, as by doing so, the edge compression effect can be partially suppressed (i.e. more light photons out of an edge crystal would hit the lower part of the diffuser's side wall in figure 4). Such an extension of the spatial dynamic range is realized by either increasing the separation between two APDs or locating the 1.5 mm width dead area at the inner regions of the module. However, a negative impact of such a configuration (dimension of diffuser/APD assembly being larger than that of the crystal array) includes the following: (1) significant light signal would be lost in the extra dead in between APDs; (2) the inter-detector crystal packing fraction will be compromised. Nevertheless, the achieved improvement in edge crystal separation through optimizing APD layout is not sufficient to completely suppress the edge compression for the block detector design under investigation.

Besides the light-sharing configuration, we also find that there is also a SNR threshold that the block detector needs to exceed in order to resolve all crystals (figure 10). The detector design based on APDs is more challenging compared to PMT-based designs due to relatively a lower SNR. In this work, we introduced the  $\text{SNR}_{\text{block}}$ , which allows us set up a link between the noise modeling and the detector's energy spectrum. The latter can be easily measured before a full block detector is built. There are several ways to improve the APD SNR such as optimizing high-voltage bias and shaping time, as well as cooling the APDs. Also note that even though  $\text{noise}_{\text{spatial}}$  is not integrated into  $\text{SNR}_{\text{block}}$  for several reasons we discussed above, it does affect both the quality of flood map (such as  $D_1$ ,  $D_2$  and  $D_3$  in figure 3) and the energy resolution of the 511 keV photopeak.

#### 4.2. Experimental study

Figure 12 indicates that the slotted diffuser designs are able to suppress the edge light spread compression more effectively than the dual layer design, which is consistent with simulation results in figure 10 and gives us the confidence in both photon transport modeling and the SNR framework we have developed in this paper. Although the simulation indicates that design II could address the edge light spread compression and enable good separation of corner crystals shown in figure 9(c), we did not see that in the experimental results in figure 12(b). We hypothesize that this is because design II suffers from a decreased SNR due to the light loss occurring at the upper portion of the optical diffuser covered by black tape (the offset from 0 to  $-2$  mm in figure 9(b)). To put it another way, the reason why this configuration cannot resolve 64 crystals might be due to the insufficient  $\text{SNR}_{\text{block}}$ , instead of the light-sharing scheme and associated level of edge light compression. If other photodetectors of a higher SNR such as

large-area SiPMs or other crystal materials with higher yield than LYSO crystal employed, we predict that design II would also yield well-separated crystals.

For designs III and IV, corner/edge crystals exhibit lower 511 keV photon sensitivity, lower gain and poorer energy resolution, compared to center crystals. The reduction of photon sensitivity is mainly due to the fact that incoming 511 keV photons are more likely to scatter and escape from edge/corner crystals without being stopped by surrounding crystals, compared to central crystals. The reduction of gain for corner/edge crystals might be attributed to two reasons. First, as slotted diffusers are used, light photons more frequently interact with internal interfaces within the diffuser prior to being detected. Such interactions cause light loss and light collection variations. Second, for edge/corner crystal elements, a larger portion of light signal is lost due to the existence of peripheral dead area compared to that of the center crystals.

For designs III and IV, both energy resolution and the time resolution measured for a center crystal element (figure 13) are inferior to those obtained using a single LYSO crystal element coupled to a single APD (figure 11). This can be attributed to the use of a thick optical diffuser causing additional light loss and the additive uncorrelated noise from four APDs. Note that time resolution results can be improved by replacing the large-area APDs studied, which were actually position-sensitive APDs (PSAPDs), by regular non-position-sensitive APDs. The former is known to introduce timing dispersion due to the presence of a resistive sheet that is employed to achieve position sensitivity. Another interesting finding is that both energy resolution and PVRs are slightly better in design III compared to design IV, which was not expected. The motivation for design IV is to introduce the tapered feature (for eight sections located at the outer regions of the diffuser) so that the light loss occurring at the dead area of APDs could be avoided. However, the difference reveals that the tapered diffuser has not improved the light collection for corner/edge crystals. A tentative explanation is as follows. When a tapered diffuser is utilized, those light photons produced from crystals hitting the tapered surface will experience a light loss at the tapered faces (i.e. total internal reflection only occurs above a certain incidence angle at the tapered face). In addition, since the diffuser end closer to crystals has larger cross-sectional area than the end closer to APDs, this will also cause light loss due to the conservation of phase space (Liouville's theorem) (Marcuse 1971). The extent of light loss is proportional to the tapered angle. Overall, the light collection efficiency is worse than a diffuser of square cross-section. Taking into account the increased complexity in manufacturing and assembling components of a tapered shape, design III is preferred over design IV.

The overlapping between adjacent peaks in figure 13(c) is due to several factors: the light-sharing ratio, the associated Poisson statistics of scintillation light photons, edge LSF compression, the noise of APDs and electronics, as well as the inter-crystal scattering among LYSO crystal array elements. These factors result in approximately a factor of 4 drop in the PVR value, when compared to the simulated  $D_3$  ( $\sim 15$ ) in figure 7(a) with a 9 mm thickness diffuser. Such information suggests that a pre-selection criterion should be applied to exclude those designs with relatively small  $D_3$  based upon formula (2).

Overall, good agreement between simulation and experimental results in this work leads us to believe that by integrating the light-sharing optimization of the LSF with the SNR analysis of APDs, we have established a reasonable framework for PET block detector design. Further validations include checking the modeling accuracy in DETECT2000 and parameters used in the SNR analysis such as leakage current and excess noise factor. Improving the accuracy of these components would enable us to further improve the accuracy of the presented framework. Furthermore, the generalized framework built in this work, if successful, will help to guide PET detector module designs for other PET configurations as well. For instance, the current

design can be used to scale down to a preclinical PET system or scale up to a whole-body clinical scanner by selecting different crystal/diffuser dimensions. System designs comprising other MRI-compatible photodetectors such as emerging SiPM devices can also benefit from the framework, as they share several design features studied in this work, including crystal array, optical diffuser, light sharing, detector dead area and SNR performance.

## 5. Conclusions

We investigated the feasibility of designing an Anger-logic PET detector module using large-area high-gain APDs for a brain-dedicated PET/MRI system. Using Monte Carlo simulation and analytical formulations, we systematically optimized the detector design, with regard to scintillation crystal element dimension, optical diffuser dimensions, surface treatment, layout of APDs, and SNR of APD devices. The model developed applies whether one scales the design down to a preclinical PET system, to scale up to a whole-body clinical scanner, or replaces APDs with other novel detectors of better timing and a higher SNR such as SiPMs. A detector prototype was built (an  $8 \times 8$  array of  $2.75 \times 3.00 \times 20$  mm<sup>3</sup> LYSO crystal elements, optical diffuser:  $22.0 \times 24.0 \times 9.0$  mm<sup>3</sup>, surface treatment: METAL). Four designs of optical diffuser were tested and two slotted diffuser designs were able to resolve all crystals within the block with good uniformity and PVR. For the block detector with the optical diffuser following design III (slotted design without tapering), the 511 keV photopeak energy resolution of the global energy spectrum is  $13.4 \pm 0.4\%$  FWHM. The measured energy resolution of all 64 crystals has a maximum value of  $17.3 \pm 0.4\%$  FWHM and a minimum value of  $11.3 \pm 0.3\%$  FWHM. The measured time resolution of the block is  $4.85 \pm 0.04$  ns FWHM (center crystal),  $5.17 \pm 0.06$  ns FWHM (edge crystal), and  $5.18 \pm 0.07$  ns FWHM (corner crystal). Time-resolution results will be improved if we were to replace the position-sensitive APDs with non-position-sensitive APDs. With the detector prototype built, we are currently working toward the incorporation of depth-of-interaction capability. Finally, using a photodetector with higher gain and faster timing capabilities, such as a large-area SiPM, such a block detector design might be useful in time-of-flight (ToF) PET/CT or ToF-PET/MR system designs, provided that the SNR is high enough.

## Acknowledgment

This work was sponsored in part by a grant from GE Healthcare.

## References

- Casey M E and Nutt R 1986 A multicrystal two dimensional BGO detector system for positron emission tomography *IEEE Trans. Nucl. Sci.* **33** 460–3
- Catana C, Procissi D, Wu Y, Judenhofer M S, Qi J, Pichler B J, Jacobs R E and Cherry S R 2008 Simultaneous *in vivo* positron emission tomography and magnetic resonance imaging *Proc. Natl Acad. Sci. USA* **105** 3705–10
- Chatziioannou A, Tai Y C, Doshi N and Cherry S R 2001 Detector development for microPET II: a  $1 \mu\text{l}$  resolution PET scanner for small animal imaging *Phys. Med. Biol.* **46** 2899–910
- Dahlbom M and Hoffman E J 1988 An evaluation of a two-dimensional array detector for high resolution PET *IEEE Trans. Med. Imaging* **7** 264–72
- German G and Hoffman E J 1990 A study of data loss and mispositioning due to pileup in 2D detectors in PET *IEEE Trans. Nucl. Sci.* **37** 671–5
- Grazioso R, Aykac M, Casey M E, Givens G and Schmand M 2005 APD performance in light sharing PET applications *IEEE Trans. Nucl. Sci.* **52** 1413–6
- Heinrichs U, Blume A, Blumann N, Engels R, Kemmerling G, Weber S and Ziemons K 2002 Statistical studies on the light output and energy resolution of small LSO single crystals with different surface treatments combined with various reflector materials *Nucl. Instrum. Methods A* **486** 60–6

- Humm J L, Rosenfeld A and Guerra A D 2003 From PET detectors to PET scanners *Eur. J. Nucl. Med.* **30** 53–9
- Joung J, Miyaoka R S and Lewellen T K 2002 cMiCE: a high resolution animal PET using continuous LSO with a statistics based positioning scheme *Nucl. Instrum. Methods A* **489** 584–98
- Judenhofer M S *et al* 2008 Simultaneous PET-MRI: a new approach for functional and morphological imaging *Nat. Med.* **14** 459–65
- Knoll G E, Knoll T E and Henderson T M 1988 Light collection scintillation detector composites for neutron detection *IEEE Trans. Nucl. Sci.* **35** 872–5
- Kolb A, Judenhofer M S, Lorenz E, Renker D and Pichler B J 2010 Evaluation of Geiger-mode APDs for PET block detector designs *Phys. Med. Biol.* **55** 1815–32
- Kwon S I *et al* 2011 Development of small-animal PET prototype using silicon photomultiplier (SiPM): initial results of phantom and animal imaging studies *J. Nucl. Med.* **52** 572–9
- Lecomte R, Cadorette J, Jouan A, Heon M, Rouleau D and Gauthier G 1990 High resolution positron emission tomography with a prototype camera based on solid state scintillation detectors *IEEE Trans. Nucl. Sci.* **37** 805–11
- Lewellen T K 2008 Recent developments in PET detector technology *Phys. Med. Biol.* **53** R287–317
- Ling T, Lee K and Miyaoka R S 2006 Performance comparisons of continuous miniature crystal element (cMiCE) detectors *IEEE Trans. Nucl. Sci.* **53** 2513–8
- Macovski A 1983 *Medical Imaging Systems* (Englewood Cliffs, NJ: Prentice-Hall)
- Marcuse D 1971 Compression of a bundle of light rays *Appl. Opt.* **10** 494–7
- Melcher C L 2000 Scintillation crystals for PET *J. Nucl. Med.* **41** 1051–5
- Moisan C, Vozza D and Loope M 1997 Simulating the performances of an LSO based position encoding detector for PET *IEEE Trans. Nucl. Sci.* **44** 2450–8
- Moszynski M, Szawlowski M, Kapusta M, Balcerzyk M and Wolski D 2000 Large area avalanche photodiodes in x-rays and light detection *IEEE Trans. Nucl. Sci.* **47** 1297–302
- Nekolla S G, Martinez-Moeller A and Saraste A 2009 PET and MRI in cardiac imaging: from validation studies to integrated applications *Eur. J. Nucl. Med. Mol. Imag.* **1** (Suppl.) 121–30
- Peng H, Handler W B, Scholl T J, Simpson P J and Chronik B A 2010a Proof-of-principle study of a small animal PET/field-cycled MRI combined system using conventional PMT technology *Nucl. Instrum. Methods A* **612** 412–20
- Peng H, Olcott P D, Spanoudaki V and Levin C S 2008 Can large-area avalanche photodiodes be used for a clinical PET/MRI block detector? *IEEE Nucl. Sci. Symp. Conf. Rec.* pp 4675–80
- Peng H, Simpson P J and Chronik B A 2010b Evaluation of a mesh photomultiplier tube for a PET/field-cycled MRI prototype *IEEE Trans. Nucl. Sci.* **57** 31–9
- Phelps M E, Mazziotta J C and Schelbert H R 1986 *Positron Emission Tomography and Autoradiography* (New York: Raven Press)
- Pichler B J, Bernecker F, Boning G, Rafecas M, Pimpl W, Schwaiger M, Lorenz E and Ziegler S I 2001 A 4 × 8 APD array, consisting of two monolithic silicon wafers, coupled to a 32-channel LSO matrix for high-resolution PET *IEEE Trans. Nucl. Sci.* **48** 1391–6
- Pichler B J, Kolb A, Nagele T and Schlemmer H P 2010 PET/MRI: paving the way for the next generation of clinical multimodality imaging applications *J. Nucl. Med.* **51** 333–6
- Rothfuss H, Casey M, Conti M, Doshi N, Eriksson L and Schmand M 2004 Monte Carlo simulation study of LSO crystals *IEEE Trans. Nucl. Sci.* **51** 770–4
- Schaart D R, Dam H T, Seifert S, Vinke R, Dendooven P, Lohner H and Beekman F J 2009 A novel, SiPM-array-based, monolithic scintillator detector for PET *Phys. Med. Biol.* **54** 3501–12
- Schlemmer H P *et al* 2008 Simultaneous MR/PET imaging of the human brain: feasibility study *Radiology* **248** 1028–35
- Shao Y, Cherry S R, Farahani K, Meadors K, Siegel S, Silverman R W and Marsden P K 1997 Simultaneous PET and MR imaging *Phys. Med. Biol.* **42** 1965–70
- Song T Y, Wu H, Siegel S and Tai Y C 2010 A sub-millimeter resolution PET detector module using a multi-pixel photon counter array *Phys. Med. Biol.* **55** 2573–87
- Takasawa M *et al* 2005 How reliable is perfusion MR in acute stroke? Validation and determination of the penumbra threshold against quantitative PET *Stroke* **39** 870–7
- Wong W H, Uribe J, Hicks K and Zambelli M 1994 A 2-dimensional detector decoding study on BGO arrays with quadrant sharing photomultipliers *IEEE Trans. Nucl. Sci.* **41** 1453–7
- Wong W H, Yokoyama S, Uribe J, Baghaei H, Li H, Wang J and Zhang N 1999 An elongated position sensitive block detector design using the PMT quadrant-sharing configuration and asymmetric light partition *IEEE Trans. Nucl. Sci.* **46** 542–5
- Ziegler S I, Pichler B J, Boening G, Rafecas M, Pimpl W, Lorenz E, Schmitz N and Schwaiger M 2001 A prototype high-resolution animal positron tomograph with avalanche photodiode arrays and LSO crystals *Eur. J. Nucl. Med.* **28** 136–43